Frontal Scale Air–Sea Interaction in High-Resolution Coupled Climate Models

FRANK O. BRYAN, ROBERT TOMAS, AND JOHN M. DENNIS

National Center for Atmospheric Research, Boulder, Colorado

DUDLEY B. CHELTON

College of Oceanic and Atmospheric Sciences, Oregon State University, Corvallis, Oregon

NORMAN G. LOEB

NASA Langley Research Center, Hampton, Virginia

JULIE L. MCCLEAN

Scripps Institution of Oceanography, La Jolla, California

(Manuscript received 8 February 2010, in final form 28 June 2010)

ABSTRACT

The emerging picture of frontal scale air–sea interaction derived from high-resolution satellite observations of surface winds and sea surface temperature (SST) provides a unique opportunity to test the fidelity of high-resolution coupled climate simulations. Initial analysis of the output of a suite of Community Climate System Model (CCSM) experiments indicates that characteristics of frontal scale ocean–atmosphere interaction, such as the positive correlation between SST and surface wind stress, are realistically captured only when the ocean component is eddy resolving. The strength of the coupling between SST and surface stress is weaker than observed, however, as has been found previously for numerical weather prediction models and other coupled climate models. The results are similar when the atmospheric component model grid resolution is doubled from 0.5° to 0.25°, an indication that shortcomings in the representation of subgrid scale atmospheric planetary boundary layer processes, rather than resolved scale processes, are responsible for the weakness of the coupling. In the coupled model solutions the response to mesoscale SST features is strongest in the atmospheric boundary layer, but there is a deeper reaching response of the atmospheric circulation apparent in free tropospheric clouds. This simulated response is shown to be consistent with satellite estimates of the relationship between mesoscale SST and all-sky albedo.

1. Introduction

Recently available high-resolution satellite observations of sea surface temperature (SST) and near surface winds have revealed fundamentally different air–sea coupling mechanisms on the scale of ocean fronts and eddies (horizontal scales of 10s to 100s of kilometers) compared to those on gyre to basin scales (Xie 2004; Chelton et al. 2004). At midlatitudes and large scales, higher surface winds tend to be associated with cool SST anomalies as a result of increased turbulent fluxes of sensible and latent heat out of the ocean and turbulent entrainment of cooler thermocline water into the surface layer; that is, the SST anomalies result from forcing by the atmosphere (e.g., Alexander et al. 2002). In contrast, at smaller spatial scales characteristic of ocean fronts and eddies, positive near surface wind anomalies are found over warm SST features, an indication that in this regime the ocean is forcing the atmosphere. Small et al. (2008) provide a recent review of the physical mechanisms involved in frontal scale air–sea interaction.

Maloney and Chelton (2006), hereafter MC06, examined the ability of a number of coupled climate system models from the International Panel on Climate Change (IPCC) Fourth Assessment Report archive to simulate the positive correlation between SST and surface wind stress magnitude on short spatial scales. They found that

Corresponding author address: Frank O. Bryan, Oceanography Section, National Center for Atmospheric Research, P.O. Box 3000, Boulder, CO 80303.
E-mail: bryan@ucar.edu

DOI: 10.1175/2010JCLI3665.1

TABLE 1. Specifications for experiments.

	Expt 1	Expt 2	Expt 3
Atmosphere resolution (horizontal/vertical)	0.5°/26 levels	0.5°/26 levels	0.25°/26 levels
Ocean Resolution (horizontal/vertical)	1.0°/60 levels	0.1°/42 levels	0.1°/42 levels
Coupling frequency	1 day	6 h	6 h
Initial conditions	2° CCSM3.5 twentieth-century expt at 1980	WOCE SAC hydrography (Gouretski and Koltermann 2004)	Year 2 of expt 2
Integration length (yr)	20	13	20
Years analyzed	1996–2000	6–10	6–10

few of the models examined were able to properly capture the essence of this relationship and, even in those that did, the magnitude of the response of the winds to SST anomalies was weak relative to observations. Most of the models were not able to simulate the basic response because their ocean component models did not have sufficient resolution to produce SST fronts on scales where the positive correlation arises. One of the models that they examined (the MIROC model) was available in high- and low-resolution versions. The high-resolution version exhibited a more robust correlation and much stronger coupling between SST and wind stress than the lower resolution version.

In this study we extend the analysis of MC06 to examine a suite of experiments carried out with the Community Climate System Model (CCSM) configured with higher resolution ocean and atmospheric components than previously available. In particular we employ a prototype version of the CCSM with an eddy-resolving ocean model (J. L. McClean et al. 2010, unpublished manuscript). Our purpose is to determine whether, and the degree to which, increased resolution in the ocean and/or atmospheric components improves the ability of the climate model to simulate air–sea interaction processes on ocean frontal scales. While relatively small scale, these processes could have much broader impacts on the global climate system. For example, strong air–sea interaction over western boundary currents is critical to the formation of subtropical mode waters and, hence, the subduction of heat anomalies and trace gases into the ocean interior (Hanawa and Talley 2001). Eastern boundary upwelling systems that support highly productive ecosystems can be strongly affected by relatively small-scale features in the wind stress distribution (Chelton et al. 2007). In atmospheric GCM simulations, Minobe et al. (2008) demonstrate that sharp SST gradients in the Gulf Stream are necessary to reproduce the observed climatological precipitation distribution, extending the influence of small-scale air–sea interaction processes throughout the depth of the troposphere. Beyond the obvious need to assess the veracity of the representation of these physical processes in the climate model, this study provides some initial insight into the quality of high-resolution coupled climate model simulations on regional scales, an area where increased attention will be directed in the forthcoming IPCC Fifth Assessment Report.

In the following section we describe the model configuration, experimental design and data processing techniques. In section 3 we present the results. In the final section we discuss the relationship of these results to other studies, and the implications for the design of next generation climate system models.

2. Methods

The model used for this study is the NCAR Community Climate System Model version 3.5 (CCSM3.5) (Neale et al. 2008; Gent et al. 2009). The atmospheric component model, the Community Atmosphere Model (CAM) is based on a finite volume discretization rather than the spectral discretization of the governing equations used in earlier versions of CAM and has extensive changes in the parameterization of subgrid-scale processes that have resulted in a significant improvement in the simulation of tropical variability relative to CCSM3.0 (Neale et al. 2008). Changes in the other component models, while less extensive, have also contributed to a reduction in systematic biases (Jochum et al. 2008; Gent et al. 2009).

Three configurations of the model are employed (Table 1). Experiment 1 is the same experiment as described in Gent et al. (2009). It uses an atmospheric component model with a zonal resolution of 0.625° and meridional resolution of 0.5°, coupled to ocean and sea ice components with a zonal resolution of 1.2° and meridional resolution varying from 0.27° at the equator to 0.54° at midlatitudes. This configuration has the same ocean resolution as used in the version of the CCSM analyzed by MC06, but the atmospheric resolution is approximately a factor of three finer. The second experiment

uses the same atmospheric component model as in experiment 1, but the ocean horizontal resolution is increased to 0.1° zonally and 0.1°cos(latitude) meridionally. This version of the ocean model, when forced with observed atmospheric conditions, produces a realistic representation of both the mean global general circulation and the distribution and magnitude of eddy variability (McClean et al. 2006; Maltrud and McClean 2005). In the final experiment, the same 0.1° ocean model is used as in experiment 2, and the atmospheric model resolution is doubled to 0.3125° longitude by 0.25° latitude.

All component models communicate via the CCSM flux coupler (Craig et al. 2005). Fluxes at the air–sea interface are calculated at 6-h intervals (daily in experiment 1) using atmospheric state variables interpolated onto the ocean model grid and conservatively remapped back to the other component model native grids. In all experiments the surface stress is computed from the relative motion of surface atmospheric winds and ocean currents. This provides an additional potential feedback process between ocean mesoscale variability and low level atmospheric flow (e.g., Small et al. 2009), though we do not investigate its role further in this study.

All model output used in this study is obtained from monthly mean sampling of the atmospheric component model, thus at that component's resolution. The monthly mean sampling available from these integrations does limit some aspects of the analysis. In particular, in the following we examine the relationship between wind stress curl and divergence with along- and crosswind components of the SST gradient. The later is nonlinear in the model variables, so should be more accurately computed instantaneously, and then the product averaged. For the purpose of this comparison, we have treated the satellite observations in the same way, forming monthly averages first, then computing products.

Following MC06, the small scale (high pass filtered) signal of interest here was isolated by subtracting fields that had been smoothed using a Loess filter with half power points at 10° latitude and 30° longitude, which is similar to a box car average with dimensions 6° latitude by 18° longitude. In the analysis of wind stress divergence and curl, the differentiation of the wind field is carried out prior to spatial filtering. To quantify relationships between the frontal scale SST features and those in wind stress, stress divergence and stress curl, we construct binned scatterplots, again following MC06. The procedure is to group data into bins 0.1°C wide according to the local high-pass SST anomaly and then calculate bin averages and bin standard deviations of wind stress, which may be plotted in a scatter diagram fashion. The slope of the least squares line fit to the bin averaged data is referred to as the coupling coefficient and serves as a means to compare simulations to one another, to satellite observations, and to previously published analyses of other models. All statistical calculations are performed using four years of monthly model output, either using all months or the four month extended seasons (May to August or November to February), the latter chosen to allow for comparison with previously published results. Statistical significance, when shown, is calculated at the 95% level using a two-sided student *t*-test.

Satellite observations of wind stress and wind speed from QuikSCAT (Chelton and Freilich 2005), SST from the Advanced Microwave Scanning Radiometer (AMSR) (Chelton and Wentz 2005), and all-sky albedo estimates from the Clouds and the Earth's Radiant Energy System (CERES) instrument (Wielicki et al. 1996) on the *Aqua* spacecraft are used to evaluate the veracity of the model simulations. The spatial filtering and time averaging are carried out in an analogous manner as described above for the model output.

3. Results

a. Surface wind response to SST

Global maps of the temporal correlation between the high-pass filtered, lowest model level (approximately 5 hPa, or about 50m, above the sea surface) wind speed and the SST are shown in Figs. 1a–c for each experiment. The correlation between high-pass filtered 10-m neutral wind speed and sea surface temperature from satellite observations is shown in Fig. 1d. There are clear differences between the simulation using the noneddy-resolving ocean component (Fig. 1a) and the two simulations using the eddy-resolving ocean component (Figs. 1b and 1c), with the latter two in far better agreement with the observations (Fig. 1d). In the experiment with the noneddy-resolving ocean (Fig. 1a), the correlation is predominantly very small or negative. In contrast, in the two experiments with the eddy-resolving ocean component (Figs. 1b–c) and in the observations (Fig. 1d), significant positive correlations emerge over regions with strong ocean eddies and fronts: the Gulf Stream and Kuroshio and their extensions, and over the path of the Antarctic Circumpolar Current in the Southern Hemisphere. The patterns of correlation in the two experiments with the eddy-resolving ocean model are very similar. There is a small increase in positive correlation in experiment 3 over experiment 2 within the latitude band of the Antarctic Circumpolar Current (by 0.1 to 0.2 in the zonal mean), but at other latitudes they are virtually the same.

The refined near-equatorial resolution in the noneddy resolving model is sufficient to allow a reasonably sharp front associated with the equatorial cold tongue and the emergence of tropical instability waves (TIWs), resulting

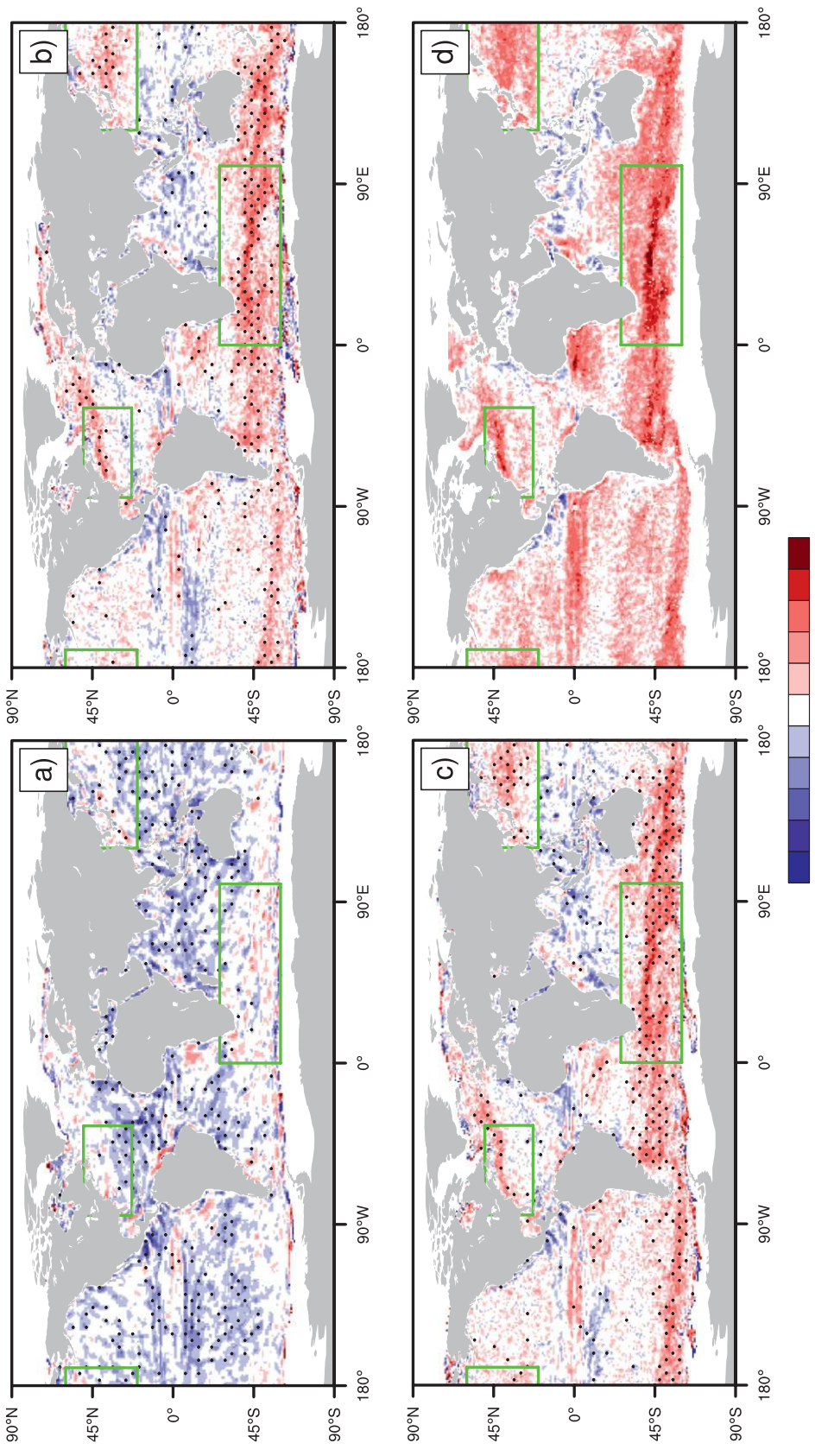

FIG. 1. Temporal correlation of high-pass filtered surface wind speed with SST. Locations where ice appeared have been masked and stippling indicates statistical significance at the 95% level calculated using a two-sided *t*-test. (a) 1.0° ocean and 0.5° atmosphere (expt 1) (b) 0.1° ocean and 0.5° atmosphere (expt 2) (c) 0.1° ocean and 0.25° atmosphere (expt 3). (d) Satellite observations. Model analysis computed using four years of monthly averaged output (48 months), observational analysis using AMSR and QuikSCAT data for 2002–2006. Green boxes delineate the regions used for the statistics presented in Table 2.

in a region of weak, but significant, positive correlation in the eastern Tropical Pacific. This feature becomes more strongly positive and more spatially extensive in the higher resolution experiments as the TIWs become better resolved. This band of positive correlation has been studied extensively (Wallace et al. 1989; Hayes et al. 1989; Xie et al. 1998; Chelton et al. 2001).

The overall negative correlation in the noneddy-resolving experiment 1 is a residual of the large-scale feedbacks as described in the introduction that still have some signature for length scales at the upper end of our filter cutoff. Reducing the filter cutoff length scale by a factor of 2 results in weaker (less negative) correlations in this experiment and stronger (more positive) correlations in the eddy resolving experiments (not shown). A few regions of significant negative correlation persist in the higher resolution simulations. Several of these are related to topographically controlled small-scale wind features such as the gap winds across the Central American isthmus (Chelton et al. 2000) and the northern end of the Mozambique Channel (Chelton et al. 2004). These same features are apparent in the observations. Other regions of negative correlation, for example, south of the equator in the central Pacific and north of the equator in the Atlantic, are positive or neutral in the observations. These appear to be the result of the overall smaller correlation (by 0.1 to 0.2 in the zonal mean) of the eddy-resolving simulations relative to observations. Both observations and the eddy-resolving experiments show a minimum in correlation in these regions. The overall positive shift of the correlations in the observations relative to the simulations is enough to account for the local sign difference.

MC06 assessed the strength of frontal-scale air–sea interaction through the magnitude of the regression coefficient of wind stress on SST for selected western boundary current regions (see also Chelton et al. 2004; O'Neill et al. 2010a; L. O'Neill et al. 2010, unpublished manuscript). The Agulhas Return Current south of Africa was one of the regions that they analyzed and has been the focus of a number of additional studies on this topic (O'Neill et al. 2003, 2005; Song et al. 2009) due to the presence of a strong topographically controlled quasi-stationary SST front and the relative remoteness from continental influences. Following the same procedures as employed by MC06, we present maps of the high-pass filtered November–February 4-yr mean SST and wind stress magnitude from the model experiments and satellite observations in Figs. 2a–d. Through this time averaging, only the stationary aspects of the SST fronts and wind stress response remain. The source of the positive correlation seen in Fig. 1: covariability of high (low) wind stress over warm (cool) SST is clear in all three experiments and in the observations. However, with the exception of the pronounced dipole structure near 80°E, the high-pass filtered fields have larger amplitude in the cases with the eddy-resolving ocean. The spatial scale of the high-pass filtered anomalies decrease, and become more realistic, with increasing ocean model resolution as expected.

Regression of wind stress magnitude on SST (Fig. 2, right panels) for the Agulhas domain shows only a weak dependence on model resolution compared to the bias relative to observations. This suggests that, within this suite of experiments, the strength of the frontal-scale air–sea coupling is controlled by atmospheric model vertical resolution or properties of the atmospheric model subgrid-scale parameterizations (which are invariant among the experiments), rather than by the resolved scale atmospheric processes. This is consistent with the regional scale atmospheric modeling study of Song et al. (2009) where the dependence of vertical mixing on static stability within the atmospheric planetary boundary layer was shown to be the primary factor controlling the strength of the coupling. However, the boundary layer parameterization used in that study was different from the one used in CCSM, so a definitive test of this conjecture will require additional sensitivity experiments with perturbed model physics at fixed horizontal resolution.

The regression analysis has also been carried out in the Gulf Stream and Kuroshio Extension regions, with the results shown in Table 2. Over each of these regions, the CCSM3.5 coupled models underestimate the regression coefficient derived from observations by a factor of 1.25–3.6. This is visibly evident in Fig. 2 where the magnitude of the SST anomalies in the eddy-resolving ocean experiments is quite comparable to observations, while the magnitude of the wind stress response remains weaker. The dependence of the regression coefficient on resolution is also small for the Northern Hemisphere boundary current regions. There is less variation in magnitude of the coupling across regions in the model than in the observations. Over each region, the bin averaged correlation increases with the increase in ocean model resolution, but there is not a significant change in the correlation with the doubling of atmospheric component resolution.

The response of the wind on crossing a SST front induces horizontal shear and divergence, depending on the angle between the wind direction and the front. The divergence of the stress is related to the local downwind component of the SST gradient and the curl of the stress is related to the crosswind component of the SST gradient (Chelton et al. 2001, 2004; MC06; O'Neill et al. 2010a; L. O'Neill et al. 2010, unpublished manuscript). The regression of wind stress curl and divergence on these components of the SST gradient are shown in

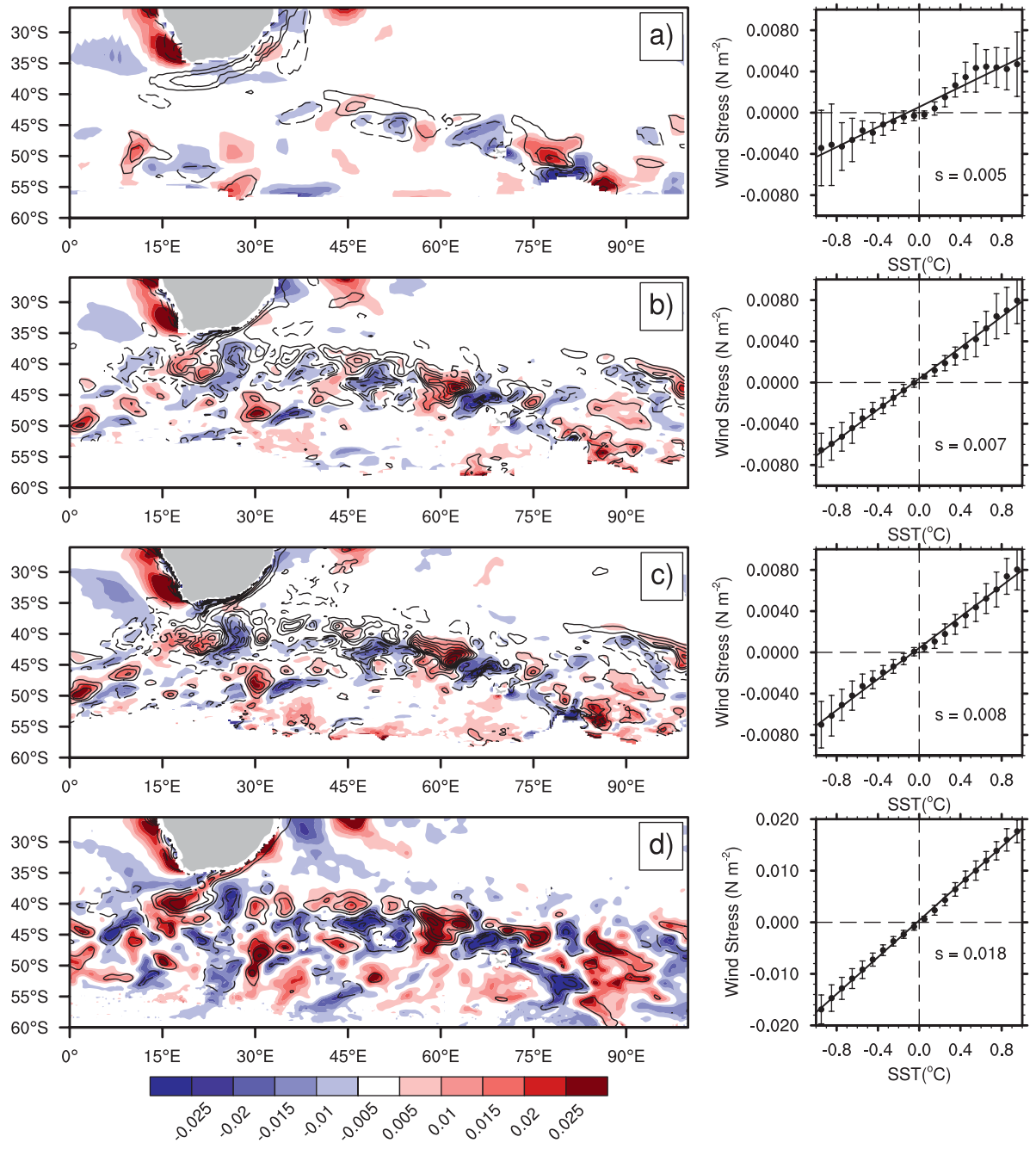

FIG. 2. (Left) High-pass filtered wind stress magnitude (color, N m^{-2}) and SST (contours, interval 0.5°C, negative values dashed). (Right) Binned scatterplots with the slope (regression coefficient) indicated. All calculations were made using four November–February seasons of monthly averaged data (16 months). Error bars are ±one std dev of the binned-monthly means. (a) 1.0° ocean and 0.5° atmosphere (expt 1) (b) 0.1° ocean and 0.5° atmosphere (expt 2) (c) 0.1° ocean and 0.25° atmosphere (expt 3). (d) Satellite observations for 2002–2006.

Table 2. For these regressions, the effect of increased resolution in the ocean component is apparent for all three regions considered. However, even for these differentiated quantities, there is not a systematic increase in the regression coefficients with increased atmospheric model resolution. As in observations, the coupling of wind stress curl and divergence is strongest over the Agulhas region. It is also noteworthy that, consistent with the satellite observations, the coupling is stronger for wind stress divergence than for wind stress curl in all

TABLE 2. Bin-averaged regression coefficients and correlations (in parentheses). Top rows: wind stress magnitude $|\boldsymbol{\tau}|$ and SST; middle rows: divergence of wind stress $\nabla \cdot \boldsymbol{\tau}$ and the downwind component of the SST gradient; bottom rows: curl of wind stress $\nabla \times \boldsymbol{\tau}$ and the crosswind component of the SST gradient. The regions, indicated by the green boxes in Fig. 1, are the Kuroshio (KE) from 20° to 60°N, 120° to 190°E; Agulhas Return Current (ARC) from 60° to 26°S, 0° to 100°E; and Gulf Stream (GS) from 23 to 50°N, 85° to 5°W. All model results are for the Nov–Feb period of the years indicated in Table 1, the QuikSCAT vs AMSR results are for 2003 through 2007.

	Region	Expt 1	Expt 2	Expt 3	QuikSCAT and AMSR
$\lvert\boldsymbol{\tau}\rvert$ and SST (Pa °C^{-1})	KE	0.007 (0.69)	0.008 (0.92)	0.006 (0.93)	0.010
	ARC	0.005 (0.82)	0.007 (0.96)	0.008 (0.96)	0.018
	GS	0.006 (0.73)	0.004 (0.78)	0.005 (0.79)	0.009
$\nabla \cdot \boldsymbol{\tau}$ and downwind ∇SST 10^2 (Pa °C^{-1})	KE	−0.16 (−0.12)	0.83 (0.95)	0.75 (0.98)	0.64
	ARC	1.02 (0.71)	1.03 (0.98)	0.99 (0.98)	1.62
	GS	0.39 (0.48)	0.60 (0.90)	0.50 (0.90)	0.62
$\nabla \times \boldsymbol{\tau}$ and crosswind ∇SST 10^2 (Pa °C^{-1})	KE	−0.51 (−0.49)	0.50 (0.89)	0.53 (0.94)	0.42
	ARC	0.75 (0.53)	0.82 (0.97)	0.84 (0.98)	1.33
	GS	−0.37 (−0.34)	0.29 (0.59)	0.33 (0.82)	0.38

three regions. This is a consequence of the SST influence on wind direction that augments the divergence while diminishing the curl compared with the responses that would be obtained if SST influenced the surface wind stress magnitude alone (O'Neill et al. 2010a).

b. Tropospheric response to SST

The investigation of ocean–atmosphere coupling in climate models by MC06 was limited to analysis of the surface wind stress and SST – quantities measurable by satellites. The eddy-resolving coupled climate model provides an opportunity to begin exploring the global three-dimensional structure of the atmospheric response to frontal scale SST anomalies. Several atmospheric variables along a zonal section centered on the Agulhas Return Current are shown in Fig. 3 for experiment 2. Several dynamical processes have been implicated in the atmospheric response to small-scale SST anomalies (Small et al. 2008), but two mechanisms have been hypothesized to be of fundamental importance. The first is vertical mixing of momentum through destabilization of the atmospheric boundary layer on the warm side of SST fronts. The second is an adjustment of the hydrostatic pressure gradient within the boundary layer to thermal anomalies. We see signatures of both mechanisms in these solutions.

There is a very close relationship between high-pass SST and atmospheric boundary layer height with a deeper boundary layer over warm SST (Figs. 3d and 3h). The boundary layer is deeper overall in winter than summer, but the close correspondence holds in both seasons. The surface temperature signal is carried through the boundary layer but does not extend very far into the troposphere in the model (Figs. 3a and 3e). The thermal anomalies tilt downwind with height as a result of advection by the large-scale westerly flow along the front, with the tilt being larger in winter as a result of the stronger winds in that season. The resulting surface pressure distribution (Figs. 3d and 3h) reflects a hydrostatic adjustment to the SST anomalies but is shifted downwind as a result of advection of the temperature signal. The vertical wind shear is reduced over warm anomalies and increased over cold anomalies, consistent with the proposed vertical mixing mechanism (Figs. 3b and 3f). Similar pressure distributions and vertical shear of the winds have been obtained from a mesoscale atmospheric model of the Agulhas Return Current region forced by observed SST (O'Neill et al. 2010b).

A deeper response in the free troposphere is apparent in cloud fraction (Figs. 3c and 3g). The small-scale positive anomalies in cloud fraction over warm SST represent a 20%–25% increase over the large-scale background fields. The deep reaching response of the cloud field appears to be related to vertical motion driven by convergence and divergence in the boundary layer, as described in more detail below. The opposite signed change in cloud fraction in the lowest level is related to relative humidity changes at the surface. While absolute humidity increases at all levels above the warm anomalies, the surface air temperature response is sufficient to create a decrease in high-pass filtered surface relative humidity with a consequent decrease in near surface cloud fraction.

Minobe et al. (2008) show that pressure adjustment of the boundary layer in the Gulf Stream region leads to low-level convergence that can connect the surface with the free troposphere through rising motion. The convergence was shown to be proportional to the Laplacian of surface pressure, which in turn is closely tied to the Laplacian of SST. We show the degree of correspondence between these quantities for the Agulhas and Gulf Stream regions and the dependence on resolution in Figs. 4 and 5. The relationship described by Minobe et al. (2008) is

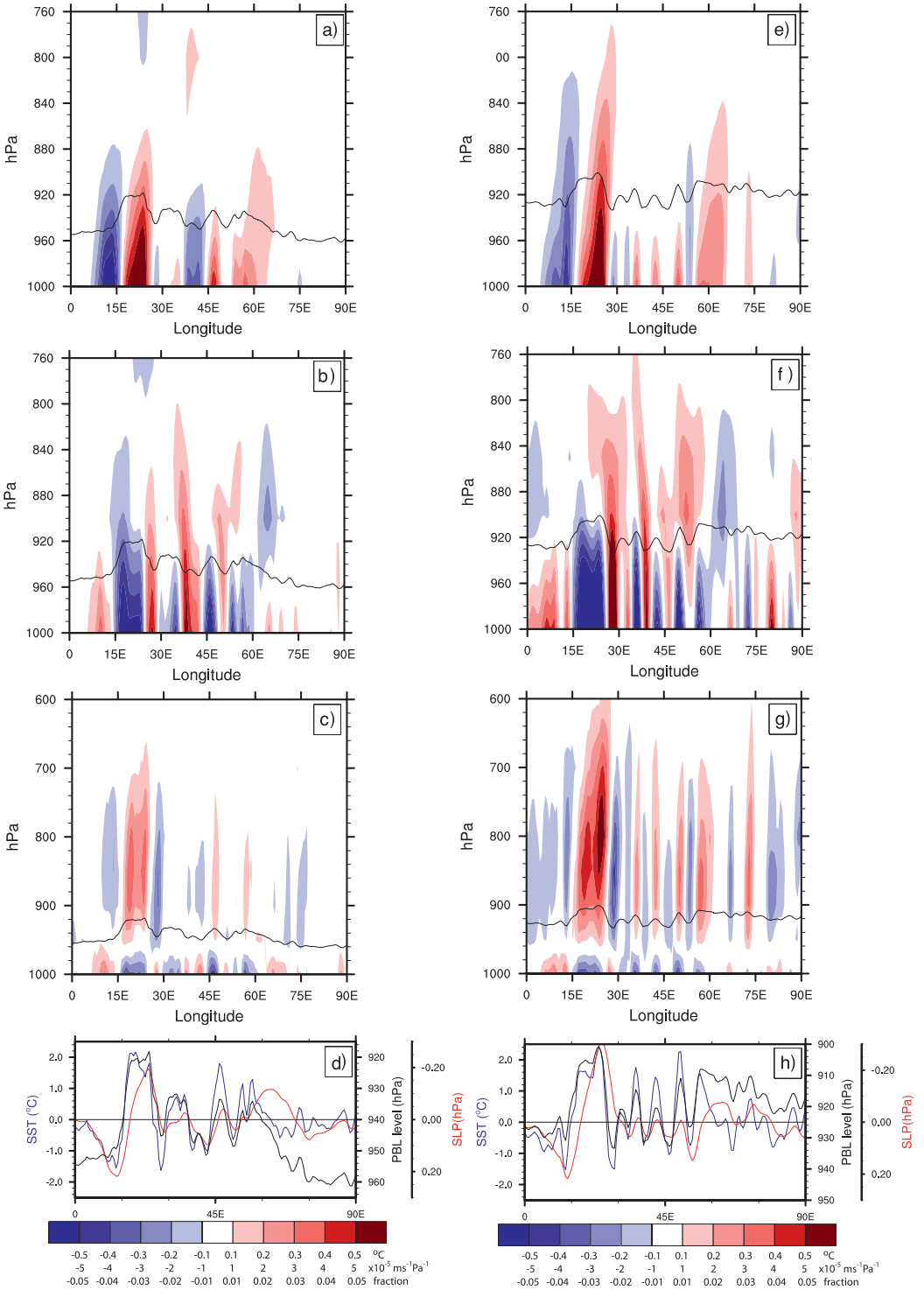

FIG. 3. Zonal–vertical cross sections along 40°S using four seasons of monthly averaged output from expt 2 (0.1° ocean and 0.5° atmosphere). Left column is for the extended summer season (Nov–Feb) and the right column is for the extended winter season (May–Aug). Solid line in each panel indicates boundary layer height. (a),(e) High-pass filtered air temperature (contour interval 0.1°C), (b),(f) High-pass filtered shear in the zonal wind ($-\partial u/\partial p$; contour interval 1×10^{-5} m s^{-1} Pa^{-1}) (c),(g) High-pass filtered cloud fraction (contour interval 0.01) (d),(h) High-pass filtered SST (blue), sea level pressure (red), and unfiltered planetary boundary layer height (black) along 40°S. Note that the vertical scale changes in the upper panels and that the scale for sea level pressure in the lowest panels is reversed.

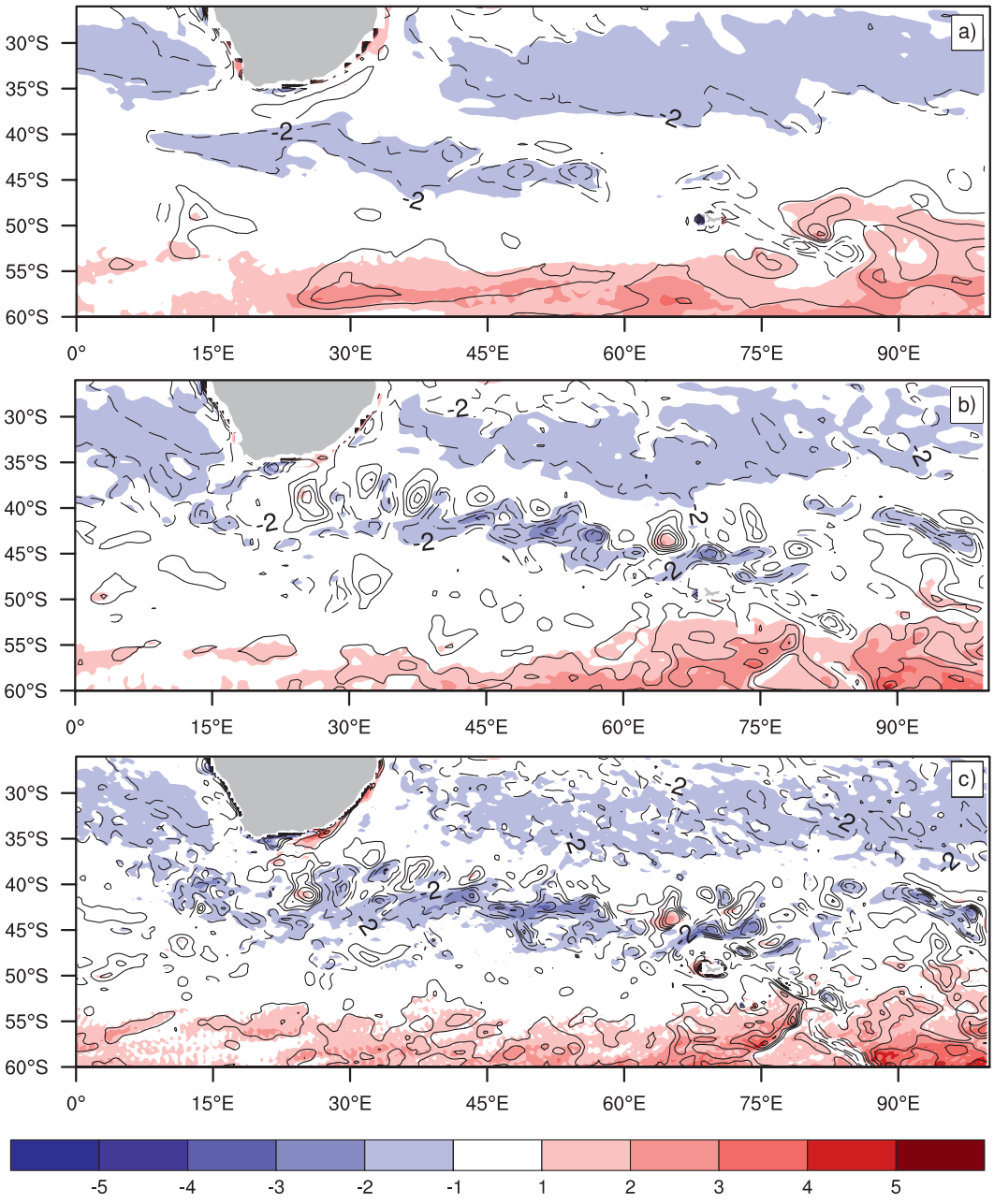

FIG. 4. Laplacian of sea level pressure (color, 10^{-9} Pa m^{-2}) and horizontal convergence of lowest model level wind (contours, interval 2×10^{-6} s^{-1}, negative values dashed) for the winter season (May-Aug) in the Agulhas region: (a) expt 1, (b) expt 2, and (c) expt 3.

apparent in both regions but much more strongly in the CCSM experiments with an eddy-resolving ocean component. For the eddy-resolving experiments, there are interesting differences in the spatial structure of the response between these two regions. In the Agulhas region, strong convergence occurs in compact regions within each meander of the current. The free tropospheric cloud response shown along 40°S in Fig. 3 is collocated with the convergence centers seen in Figs. 4b–c. The strength of the convergence centers does not increase significantly with the increase in atmospheric model resolution. In the Gulf Stream region, the model response for the eddy-resolving cases (Figs. 5b and 5c) is very similar to the result of Minobe et al. (2008) obtained from ECMWF reanalysis data. There is a coherent band of strong convergence along the warm side of the Gulf Stream front with an inshore region of divergence. In this region, during the winter period considered here, the ambient wind

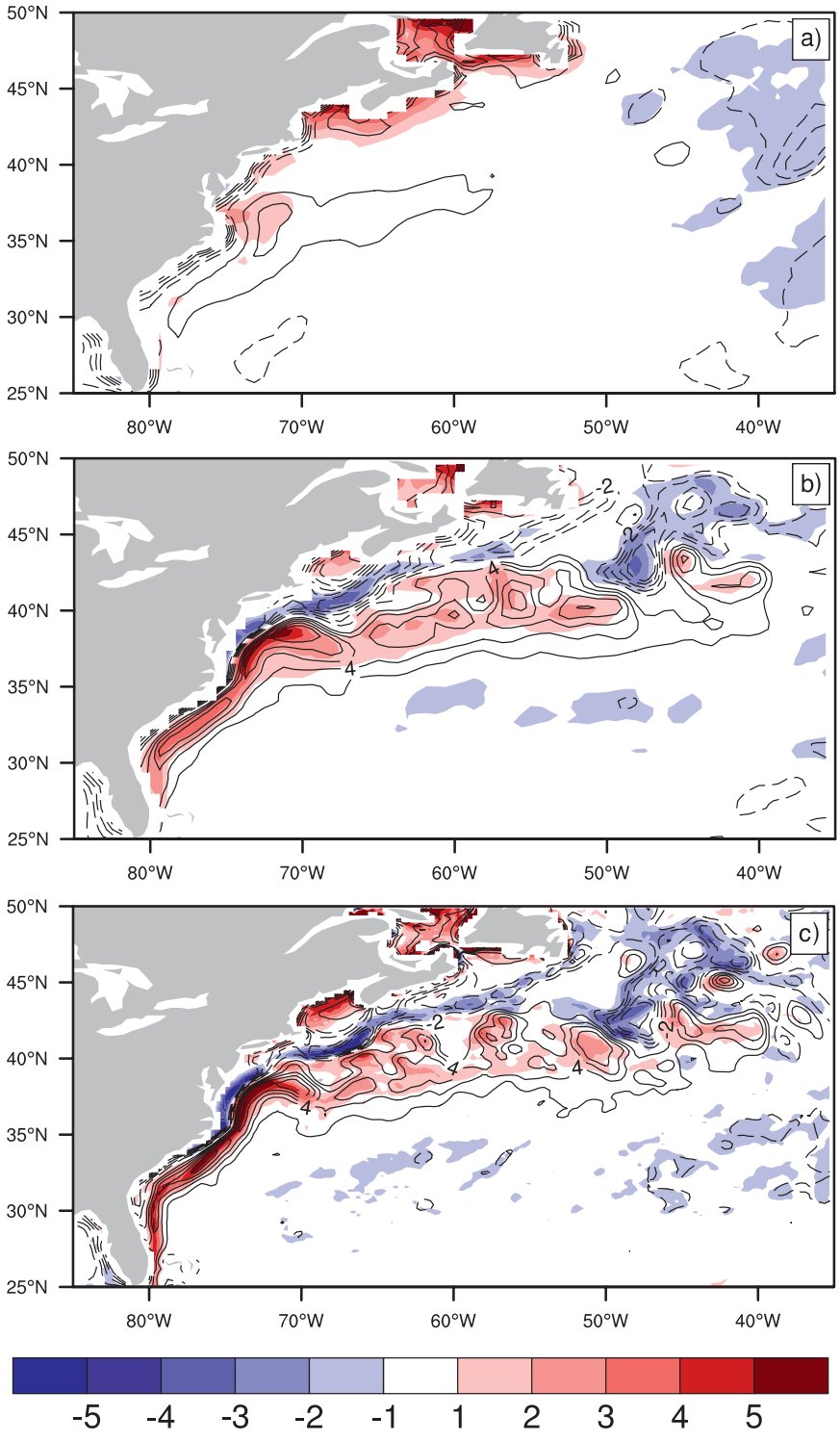

FIG. 5. As in Fig. 4 but for the winter season (Nov–Feb) in the Gulf Stream region.

direction is northwesterly, so there is a broad connected band where the downwind SST gradient has the same sign. In contrast, in the Agulhas the wind direction is closely aligned with the mean axis of the front and the downwind SST gradient alternates in sign across each meander, resulting in the more isolated convergence centers.

A consequence of the increase in free tropospheric cloud over warm SST anomalies is a decrease in shortwave

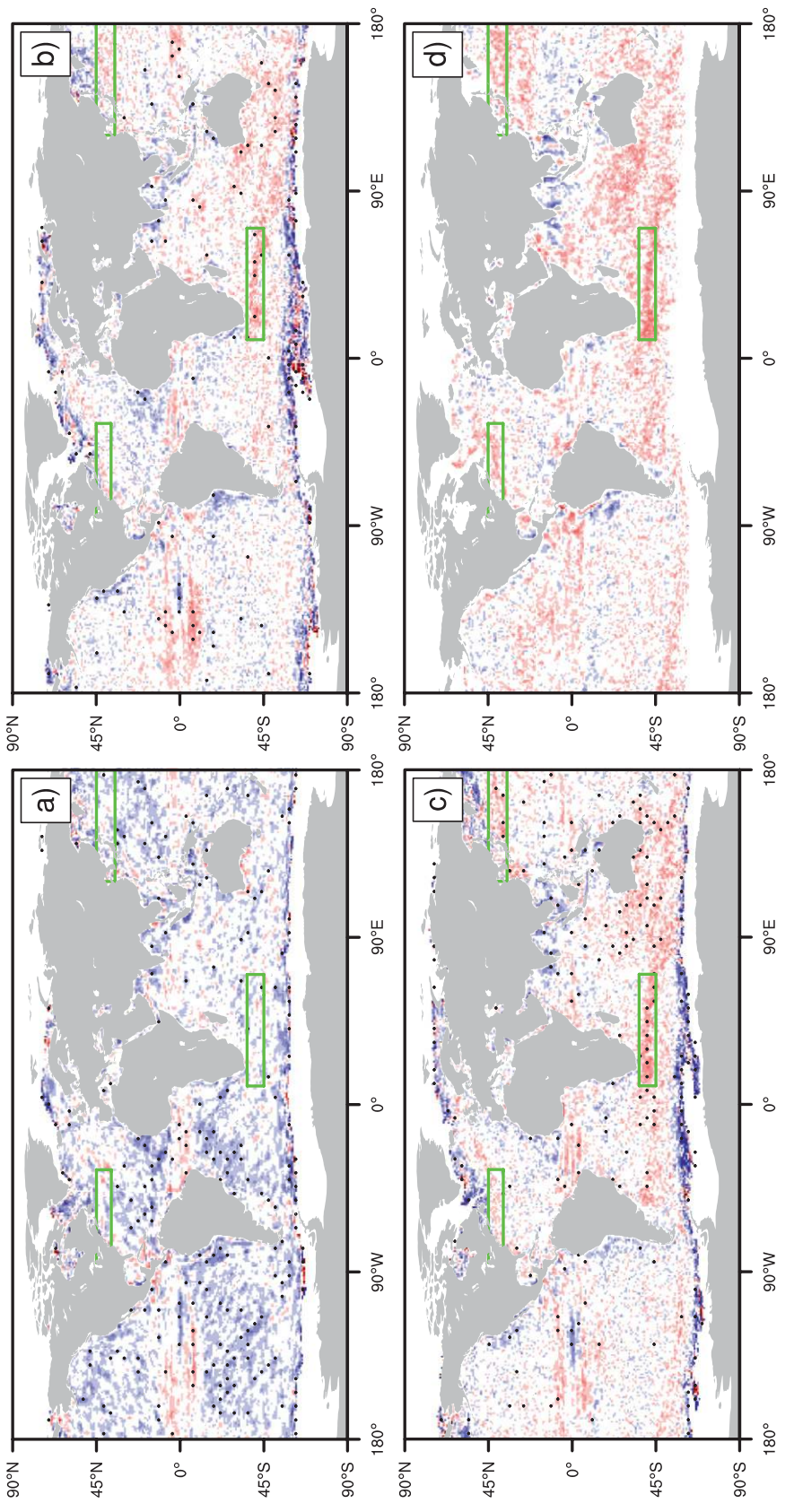

FIG. 6. Temporal correlation of high-pass filtered planetary albedo with SST. The correlations were computed using four years of monthly averaged data (48 months). Locations where ice appeared have been masked and stippling indicates statistical significance at the 95% level calculated using a two-sided *t* test. (a) 1.0° ocean and 0.5° atmosphere (expt 1); (b) 0.1° ocean and 0.5° atmosphere (expt 2); (c) 0.1° ocean and 0.25° atmosphere (expt 3); and (d) AMSR SST and CERES albedo satellite observations. Green boxes delineate the regions used for the statistics presented in Table 3.

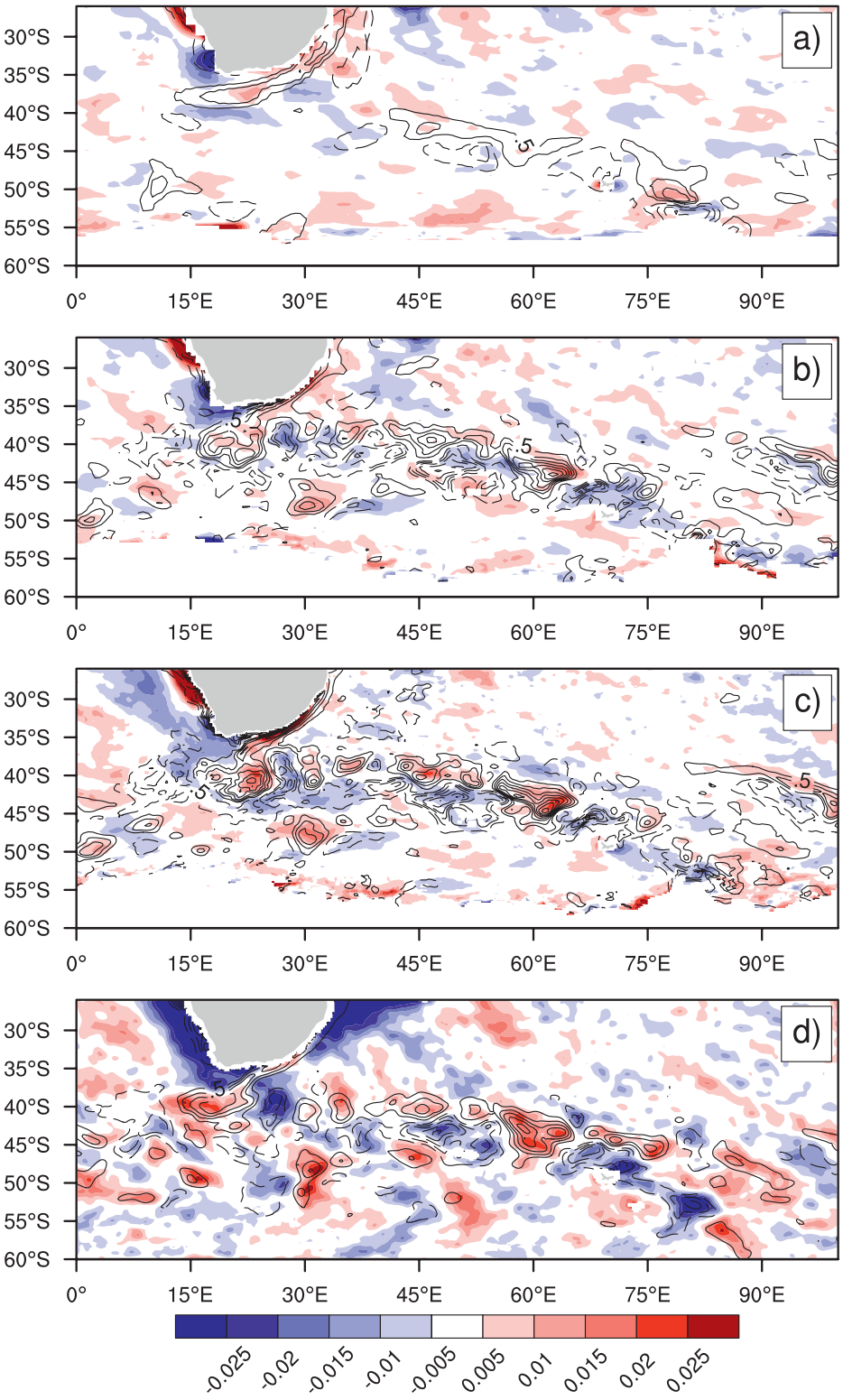

FIG. 7. High-pass filtered all-sky albedo (color) and SST (contours, interval 0.5°C, negative values dashed). All calculations were made using four Nov–Feb seasons of monthly averaged data (16 months). (a) 1.0° ocean and 0.5° atmosphere (expt 1); (b) 0.1° ocean and 0.5° atmosphere (expt 2); (c) 0.1° ocean and 0.25° atmosphere (expt 3); and (d) AMSR SST and CERES albedo satellite observations.

radiative flux reaching the sea surface. This appears as a positive correlation between high-pass filtered albedo and SST in the experiments with eddy-resolving oceans (Figs. 6b–c), as well as in the CERES satellite observations (Fig. 6d), but is absent in the experiment with lower ocean resolution (Fig. 6a). This response is clearest over the Agulhas Return Current region. The spatial structure of the relationship between these quantities is shown in Figs. 7a–c for the model experiments and in Fig. 7d for satellite observations. As in the case of the response of surface winds, while capturing the correct sign of the relationship, the model underestimates the magnitude of the response of albedo to SST features.

This cloud effect on shortwave radiation reaching the sea surface represents a negative feedback on small-scale SST anomalies that is only present when the ocean model is eddy resolving. The midsummer top-of-atmosphere downward solar flux at 40°S is 515 W m^{-2}, so a 2% change in albedo representative of the larger meanders in the Agulhas Return Current would result in a change in solar radiation reaching the surface of approximately 10 W m^{-2}. The relative contribution of this feedback to the surface energy balance is quantified by regression of high-pass filtered surface energy flux components on SST for the major frontal regions (Table 3). For experiment 1, the regression between solar flux and SST is positive in all three regions – larger solar fluxes drive higher SST. In contrast, for experiment 3, the regression coefficients are negative for all three regions – higher SST is driving weaker solar fluxes. The difference between experiments for the solar flux feedback is greatest in the Agulhas region with a change in the feedback parameter of 14.3 W m^{-2} K^{-1}. There is change in the latent heat flux feedback with increasing resolution of comparable magnitude and a modest change in the sensible heat flux feedback. However, the solar radiation feedback is the only term in the frontal scale surface energy balance that changes sign across model resolutions. Latent and sensible heat flux feedbacks are negative and become more negative with increasing resolution.

TABLE 3. Area-averaged simultaneous regression coefficients of high-pass filtered, nonseasonal, surface energy flux components on sea surface temperature (W m^{-2} °C^{-1}). SW – net short wave radiation; LW – net long wave radiation; LH – turbulent latent heat flux; SH – turbulent sensible heat flux. Fluxes are considered positive from the atmosphere downward into the surface. Regions, green boxes in Fig. 6, are the Kuroshio (KE) from 35° to 45°N, 120°E–180°; Agulhas Return Current (ARC) from 45° to 36°S; and Gulf Stream (GS) from 37° to 45°N, 85° to 35°W. All model results are for the 48-month period indicated in Table 1.

Region	Flux component	Expt 1	Expt 2	Expt 3
KE	SW	5.4 ± 4.8	−0.1 ± 1.3	−0.4 ± 1.2
	LW	−3.0 ± 1.9	−2.7 ± 0.6	−2.7 ± 0.5
	LH	−14.9 ± 3.5	−23.5 ± 1.7	−23.9 ± 1.6
	SH	−6.2 ± 1.9	−11.0 ± 1.1	−11.0 ± 1.0
GS	SW	4.3 ± 5.1	0.7 ± 1.4	−0.1 ± 1.3
	LW	−3.0 ± 2.3	−3.1 ± 0.6	−2.9 ± 0.6
	LH	−13.1 ± 3.7	−23.9 ± 2.0	−23.7 ± 1.7
	SH	−5.0 ± 1.8	−9.0 ± 1.0	−9.1 ± 0.9
ARC	SW	12.8 ± 8.9	−1.0 ± 1.2	−1.5 ± 1.3
	LW	−5.1 ± 3.7	−2.6 ± 0.5	−2.5 ± 0.5
	LH	−16.3 ± 5.1	−25.8 ± 1.2	−25.7 ± 1.3
	SH	−5.9 ± 2.1	−10.3 ± 0.6	−10.0 ± 0.6

4. Conclusions

Coupled climate system models in which the ocean component is eddy-resolving are on the horizon. The experiments presented here demonstrate that there is a fundamental change in the character of the coupling between the lower atmosphere and the sea surface in this class of models as compared to earlier models in which the ocean is not eddy resolving. A more realistic pattern of positive correlation between small-scale features in SST and low-level wind speed and stress emerges over ocean regions with strong fronts and mesoscale eddies. Despite this improvement in the distribution and pattern of this response, the strength of the coupling as measured by the regression coefficient of wind stress (and its divergence and curl) remains weaker than observed, with little change across atmospheric model resolutions. This is suggestive of remaining shortcomings in the representation of boundary layer processes in the atmospheric component model, which was previously shown to be the case for other models (Song et al. 2009). This dependence provides an additional constraint for assessing the veracity of the representation of these physical processes in next generation atmospheric and coupled climate models.

Analysis of the eddy-resolving coupled model simulations revealed a heretofore unappreciated signature of the atmospheric response to mesoscale SST features in the midlevel cloud and albedo distributions. While SST influence on clouds has been shown to occur over several strong SST fronts (e.g., Wai and Stage 1989; Deser et al. 1993; Hashizume et al. 2001; Minobe et al. 2008; Tokinaga et al. 2009), this has not previously been observed globally over the open ocean. The relationship between mesoscale SST and all-sky albedo detected in the model has been confirmed through an analysis of CERES albedo observations. The modified response of the cloud field results in a change in the sign of the feedback between frontal scale SST features and net surface solar flux.

The relatively short length of these prototype integrations precludes a more in-depth study of the large-scale and lower-frequency implications of this new class of interaction on the global climate system. As longer experiments become computationally feasible, it will become possible to examine how the more realistic representation of near-surface processes feedback on the interior circulation of both the atmosphere and ocean.

Acknowledgments. We thank David Bailey, Tony Craig, Detelina Ivanova, Art Mirin, Nancy Norton, and Mariana Vertenstein for their assistance in configuring and running these experiments. Computing time for the experiments described in this paper was provided by the Department of Energy as part of the Multiprogramatic and Institutional Computing Initiative at Lawrence Livermore National Laboratory (LLNL), under the Office of Science (BER), U.S. Department of Energy, through Cooperative Agreement DE-FC02-97ER62402 at the National Energy Supercomputing Center, and by NCAR. FOB, RT, and JD are supported through National Science Foundation Cooperative Grant NSF01, which funds NCAR. JD was additionally supported by NSF Grants OCI-0749206 and OCE-0825754 and the Department of Energy, through CCPP Program Grant DE-PS02-07ER07-06. DBC was supported by NASA Grant NAS5-32965 for funding of Ocean Vector Winds Science Team activities. JLM was supported by the DOE, CCPP Program Grant DE-FG02-05ER64119, and an LLNL subcontract.

REFERENCES

Alexander, M. A., I. Bladé, M. Newman, J. R. Lanzante, N. C. Lau, and J. D. Scott, 2002: The atmospheric bridge: The influence of ENSO teleconnections on air–sea interaction over the global oceans. *J. Climate,* **15,** 2205–2231.

Chelton, D. B., and M. H. Freilich, 2005: Scatterometer-based assessment of 10-m wind analyses from the operational ECMWF and NCEP numerical weather prediction models. *Mon. Wea. Rev.,* **133,** 409–429.

——, and F. J. Wentz, 2005: Global microwave satellite observations of sea surface temperature for numerical weather prediction and climate research. *Bull. Amer. Meteor. Soc.,* **86,** 1097–1115.

——, M. H. Freilich, and S. K. Esbensen, 2000: Satellite observations of the wind jets off of the Pacific coast of Central America. Part I: Case studies and dynamical considerations. *Mon. Wea. Rev.,* **128,** 2019–2043.

——, and Coauthors, 2001: Observations of coupling between surface wind stress and sea surface temperature in the eastern tropical Pacific. *J. Climate,* **14,** 1479–1498.

——, M. G. Schlax, M. H. Freilich, and R. F. Milliff, 2004: Satellite measurements reveal persistent small-scale features in ocean winds. *Science,* **303,** 978–983.

——, ——, and R. M. Samelson, 2007: Summertime coupling between sea surface temperature and wind stress in the California Current System. *J. Phys. Oceanogr.,* **37,** 495–517.

Craig, A. P., R. Jacob, B. Kauffman, T. Bettge, J. Larson, E. Ong, C. Ding, and Y. He, 2005: CPL6: The new extensible, high performance parallel coupler for the Community Climate System Model. *High Perform. Comput. Appl.,* **19,** 309–328.

Deser, C., J. J. Bates, and S. Wahl, 1993: The influence of sea surface temperature gradients on stratiform cloudiness along the equatorial front in the Pacific Ocean. *J. Climate,* **6,** 1172–1180.

Gent, P. R., S. G. Yeager, R. B. Neale, S. Levis, and D. A. Bailey, 2009: Improvements in a half degree atmosphere/land version of the CCSM. *Climate Dyn.,* **34,** 819–833.

Gouretski, V. V., and K. P. Koltermann, 2004: WOCE global hydrographic climatology. Berichte des Bundesamtes für Seeschiffahrt un Hydrographie Tech. Rep. 35, Hamburg, Germany, 50 pp + 2 CD-ROM.

Hanawa, K., and L. D. Talley, 2001: Mode waters. *Ocean Circulation and Climate,* G. Siedlet, J. Church, and J. Gould, Eds., Academic Press, 373–386.

Hashizume, H., S.-P. Xie, W. T. Liu, and K. Takeuchi, 2001: Local and remote atmospheric response to tropical instability waves: A global view from space. *J. Geophys. Res.,* **106,** 10 173–10 185.

Hayes, S. P., M. J. McPhaden, and J. M. Wallace, 1989: The influence of sea surface temperature on surface wind in the eastern equatorial Pacific: Weekly to monthly variability. *J. Climate,* **2,** 1500–1506.

Jochum, M., G. Danabasoglu, M. Holland, Y.-O. Kwon, and W. Large, 2008: Ocean viscosity and climate. *J. Geophys. Res.,* **113,** C06017, doi:10.1029/2007JC004515.

Maloney, E. D., and D. B. Chelton, 2006: An assessment of sea surface temperature influence on surface winds in numerical weather prediction and climate models. *J. Climate,* **19,** 2743–2762.

Maltrud, M. E., and J. L. McClean, 2005: An eddy resolving global 1/10° ocean simulation. *Ocean Modell.,* **8,** 31–54.

McClean, J. L., M. E. Maltrud, and F. O. Bryan, 2006: Measures of the fidelity of eddying ocean models. *Oceanography,* **19,** 104–117.

Minobe, S., A. Kuwano-Yoshida, N. Komori, S.-P. Xie, and R. J. Small, 2008: Influence of the Gulf Stream on the troposphere. *Science,* **452,** doi:10.1038/Nature06690.

Neale, R. B., J. H. Richter, and M. Jochum, 2008: The impact of convection on ENSO: From a delayed oscillator to a series of events. *J. Climate,* **21,** 5904–5924.

O'Neill, L. W., D. B. Chelton, and S. K. Esbensen, 2003: Observations of SST-induced perturbations on the wind stress field over the Southern Ocean on seasonal timescales. *J. Climate,* **16,** 2340–2354.

——, ——, ——, and F. J. Wentz, 2005: High-resolution satellite measurements of the atmospheric boundary layer response to SST perturbations over the Agulhas Return Current. *J. Climate,* **18,** 2706–2733.

——, ——, and ——, 2010a: The effects of SST-induced surface wind speed and direction gradients on midlatitude surface vorticity and divergence. *J. Climate,* **23,** 255–281.

——, S. K. Esbensen, N. Thum, R. M. Samelson, and D. B. Chelton, 2010b: Dynamical analysis of the boundary layer and surface wind responses to mesoscale SST perturbations. *J. Climate,* **23,** 559–581.

Small, R. J., and Coauthors, 2008: Air–sea interaction over ocean fronts and eddies. *Dyn. Atmos. Oceans,* **45,** 274–319.

——, K. J. Richards, S.-P. Xie, P. Dutrieux, and T. Miyama, 2009: Damping of tropical instability waves caused by the action of

surface currents on stress. *J. Geophys. Res.,* **114,** C04009, doi:10.1029/2008JC005147.

Song, Q., D. B. Chelton, S. K. Esbensen, N. Thum, and L. W. O'Neill, 2009: On the coupling between sea surface temperature and low-level winds in mesoscale numerical models. *J. Climate,* **22,** 146–164.

Tokinaga, H., Y. Tanimoto, S.-P. Xie, K. Sampe, H. Tomita, and H. Ichikawa, 2009: Ocean frontal effects on the vertical development of clouds over the western North Pacific: In situ and satellite observations. *J. Climate,* **22,** 4241–4260.

Wai, W. M., and S. A. Stage, 1989: Dynamical analysis of marine atmospheric boundary layer structure near the Gulf Stream oceanic front. *Quart. J. Roy. Meteor. Soc.,* **115,** 29–44.

Wallace, J. M., T. P. Mitchell, and C. Deser, 1989: The influence of sea surface temperature on surface wind in the eastern equatorial Pacific: Seasonal and interannual variability. *J. Climate,* **2,** 1492–1499.

Wielicki, B. A., B. R. Barkstrom, E. F. Harrison, R. B. Lee III, G. L. Smith, and J. E. Cooper, 1996: Clouds and the Earth's Radiant Energy System (CERES): An Earth Observing System experiment. *Bull. Amer. Meteor. Soc.,* **77,** 853–868.

Xie, S.-P., 2004: Satellite observations of cool ocean–atmosphere interaction. *Bull. Amer. Meteor. Soc.,* **85,** 195–208.

——, M. Ishiwatari, H. Hashizume, and K. Takeuchi, 1998: Coupled ocean–atmospheric waves on the equatorial front. *Geophys. Res. Lett.,* **25,** 3863–3866.